Exploring the governing transport mechanisms of corrosive agents in a Canadian deep geological repository

Science of the Total Environment 828 (2022) 153944

Contents lists available at ScienceDirect

Science of the Total Environment

journal homepage: www.elsevier.com/locate/scitotenv

Exploring the governing transport mechanisms of corrosive agents in a Canadian deep geological repository

Tarek L. Rashwan [a], Md. Abdullah Asad [a], Ian L. Molnar [b], Mehran Behazin [c], Peter G. Keech [c], Magdalena M. Krol [a,*]

[a] Department of Civil Engineering, Lassonde School of Engineering, York University, Toronto, Ontario M3J 1P3, Canada
[b] School of Geosciences, University of Edinburgh, Edinburgh, Scotland EH8 8AQ, United Kingdom
[c] Nuclear Waste Management Organization, Toronto, Ontario M4T 2S3, Canada

HIGHLIGHTS

- Numerical modelling study of Canada's proposed deep geological repository (DGR)
- 3D model domain coupled heat transfer, unsaturated flow, and HS^- transport
- Unsaturated regions restricted and heating accelerated HS^- transport, respectively
- Saturation and heating only affected HS^- corrosion by <1% and <20%, respectively
- HS^- corrosion rates are well-predicted using simplified DGR design parameters.

GRAPHICAL ABSTRACT

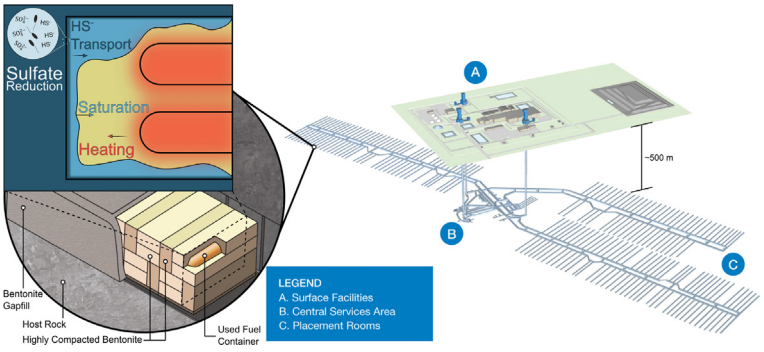

ARTICLE INFO

Article history:
Received 15 October 2021
Received in revised form 4 January 2022
Accepted 13 February 2022
Available online 19 February 2022

Editor: Christian Herrera

Keywords:
Deep geological repository
Used nuclear fuel
Numerical modelling
Thermal-hydraulic-chemical
Bentonite
Bisulfide

ABSTRACT

All nuclear energy producing nations face a common challenge associated with the long-term solution for their used nuclear fuel. After decades of research, many nuclear safety agencies worldwide agree that deep geological repositories (DGRs) are appropriate long-term solutions to protect the biosphere. The Canadian DGR is planned in either stable crystalline or sedimentary host rock (depending on the final site location) to house the used nuclear fuel in copper-coated used fuel containers (UFCs) surrounded by highly compacted bentonite. The copper-coating and bentonite provide robust protection against many corrosion processes anticipated in the DGR. However, it is possible that bisulfide (HS^-) produced near the host rock-bentonite interface may transport through the bentonite and corrode the UFCs during the DGR design life (i.e., one million years); although container performance assessments typically account for this process, while maintaining container integrity. Because the DGR design life far exceeds those of practical experimentation, there is a need for robust numerical models to forecast HS^- transport. In this paper we present the development of a coupled 3D thermal-hydraulic-chemical model to explore the impact of key coupled physics on HS^- transport in the proposed Canadian DGR. These simulations reveal that, although saturation delayed and heating accelerated HS^- transport over the first 100s and 10,000s of years, respectively, these times of influence were small compared to the long DGR design life. Consequently, the influence from heating only increased total projected HS^- corrosion by <20% and the influence from saturation had a negligible impact (<1%). By comparing the corrosion rate results with a simplified model, it was shown that nearly-steady DGR design parameters governed most of the projected HS^- corrosion. Therefore, those parameters need to be carefully resolved to reliably forecast the extent of HS^- corrosion.

* Corresponding author.
E-mail addresses: trashwan@yorku.ca (T.L. Rashwan), aasad@yorku.ca (M.A. Asad), ian.molnar@ed.ac.uk (I.L. Molnar), mbehazin@nwmo.ca (M. Behazin), pkeech@nwmo.ca (P.G. Keech), magdalena.krol@lassonde.yorku.ca (M.M. Krol).

http://dx.doi.org/10.1016/j.scitotenv.2022.153944

Nomenclature

Abbreviations

C	chemical
Cu	copper
DGR	deep geological repository
H	hydraulic
HS^-	bisulfide
MIC	microbiologically-influenced corrosion
NWMO	Nuclear Waste Management Organization
T	thermal
UFC	used fuel container

Latin letters

A_f	geometry factor, −
C	concentration, mol m^{-3}
C_0	constant boundary concentration, mol m^{-3}
C_m	specific moisture capacity, −
C_p	specific heat capacity, J kg^{-1} K^{-1}
d_p	average pore/particle diameter, m
dx/dt_{corr}	rate of corrosion, m s^{-1}
D_e	effective diffusion coefficient, m^2 s^{-1}
D_o	pore water diffusion coefficient, m^2 s^{-1}
f_{HS}	stoichiometric coefficient, −
g	gravity constant, m s^{-2}
H_p	pressure head, m
k	isotropic intrinsic permeability, m^2
k_h	anisotropic intrinsic permeability (horizontal), m^2
k_v	anisotropic intrinsic permeability (vertical), m^2
k_r	relative permeability parameter, −
L	straight-line length in porous medium, m
L_e	actual travel length in porous medium, m
m	van Genuchten parameter (1), −
M	molar mass, kg mol^{-1}
n	van Genuchten parameter (2), −
$\dot{N}''$	molar flux, mol m^{-2} s^{-1}
p	pressure, Pa
p_w	water pressure, Pa
Pe_C	Peclet number (chemical-transport), −
Pe_T	Peclet number (thermal-transport), −
q	volumetric generation term, W m^{-3}
S	saturation, −
S_e	effective saturation, $S_e = (S - S_r)/(S_f - S_r)$, −
S_f	full saturation, −
S_r	residual saturation, −
S_y	storage coefficient, −
t_c	characteristic time, s
T	temperature, K
v_D	Darcy velocity, m s^{-1}
x_c	characteristic distance, m
x_f	diffusion distance, m
z	elevation head, m

Greek symbols

α	van Genuchten parameter (3), −
δ	pore constrictivity, −
λ	thermal conductivity, W m^{-1} K^{-1}
μ	dynamic viscosity, Pa·s
ρ	density, kg m^{-3}
τ	tortuosity, −
ϕ	porosity, −
ϕ_e	diffusion-accessible porosity, −

Subscripts

avg	average
aq	aqueous phase
b	bentonite
crys	crystalline model
eff	effective (volume averaged)
g	gas phase
i	direction (x, y, z)
s	solid phase
sed	sedimentary model
w	water
0	initial

1. Introduction

Given the immediacy of climate change, energy generation systems worldwide are evolving to minimize their carbon emissions. Nuclear energy plays an important role in this evolution, as it is a mature technology that can reliably meet current energy demands with a very low carbon footprint (Ewing, 2015). However, nuclear waste management is a key issue that is currently being investigated by nuclear producing nations worldwide. Deep geological repositories (DGRs) consist of a multibarrier system, designed to safely house used nuclear fuels in copper-coated used fuel containers (UFCs) for hundreds of thousands of years deep within stable host rock formations. Many nuclear safety agencies agree that DGRs are viable and scientifically sound end-of-life solutions (Ewing, 2015; Hall et al., 2021). In Canada, the Nuclear Waste Management Organization (NWMO) is responsible for the design and execution of Canada's DGR, which consists of copper-coated carbon steel UFCs being placed within a high-density bentonite buffer surrounded by natural host rock. As the design life for these systems far exceeds the timescales of practical experimentation, there is a need for robust numerical models to aid in long-term predictions.

One concern with the long-term integrity of Canada's DGR is the potential for corrosion (through oxic, anoxic, radiation-induced, and microbiologically-influenced processes) to compromise integrity of the UFCs (Hall et al., 2021; Keech et al., 2021). Therefore, the NWMO plans to coat the UFCs with copper to prevent corrosion and surround them with highly compacted bentonite embedded within a stable, low-permeability host rock (i.e., either crystalline or sedimentary, depending on the final site location) (Hall and Keech, 2017). Although containers and geologies differ internationally, this long-term storage approach is consistent with current best practices proposed by other nuclear safety agencies, e.g., Sweden (SKB), Finland (Posiva), Switzerland (Nagra), United States (US DOE), and the United Kingdom (NDA) (Hall et al., 2021).

Of the various corrosion processes anticipated in the DGR, microbiologically-influenced corrosion (MIC) poses the most uncertainty (Hall et al., 2021). While previous research has shown that microbiological activity is minimized at average bentonite densities greater than 1600 kg m^{-3}, the interface between bentonite and host rock may foster conditions that promote sulfate-reducing microbiological activity (Bengtsson and Pedersen, 2016; Kiczka et al., 2021; Stroes-Gascoyne, 2010; Stroes-Gascoyne et al., 2011). Therefore, bisulfide (HS^-) can potentially be produced from sulfate-reducing bacteria at this interface, transport through the bentonite, and cause corrosion of the UFC copper surface following Eq. (1) (Hall et al., 2021):

$$2Cu_{(s)} + HS^-_{(aq)} + H^+_{(aq)} \rightarrow Cu_2S_{(s)} + H_{2(g)} \quad (1)$$

While an extensive research program has explored the chemical processes involved in MIC (Hall et al., 2021; Hall and Keech, 2017; Hall et al., 2018; Keech et al., 2021; Martino et al., 2014), much less research has targeted the transport processes involved for the Canadian DGR layout.

However, HS^- transport to the copper surface throughout the DGR design life (i.e., one million years) is anticipated to govern the extent of MIC and therefore also needs to be investigated (King et al., 2017a).

Many researchers have developed numerical and mathematical models to predict the long-term behaviour in various DGR designs (Birkholzer et al., 2019; Guo and Fall, 2021; Steefel et al., 2015). These models couple thermal (Baumgartner et al., 1994; Guo, 2017), hydraulic (Cleall et al., 2006; Zhou et al., 2021), mechanical (Ballarini et al., 2017; Rutqvist et al., 2002), and chemical (Huang et al., 2021; Nasir et al., 2015) processes. While these models do not specifically target HS^- transport, they do provide valuable insight regarding which key processes are likely to affect HS^- transport in a DGR. Fig. 1 illustrates a conceptual model of these key processes that are anticipated to affect HS^- transport and the characteristic evolutions in temperature, oxygen concentration, and saturation anticipated in the DGR (Hall et al., 2021; King et al., 2017b; King et al., 2008). Fig. 1a illustrates a conceptual snapshot of the temperature and saturation distribution anticipated in the early-life of the DGR (i.e., in the first 10s–100s of years). Fig. 1b illustrates the envelopes of anticipated average DGR temperature and oxygen evolutions, which shows the DGR is expected to exhibit oxic conditions over the first 10s to 100s of years and be at elevated temperatures for the first 100,000 years.

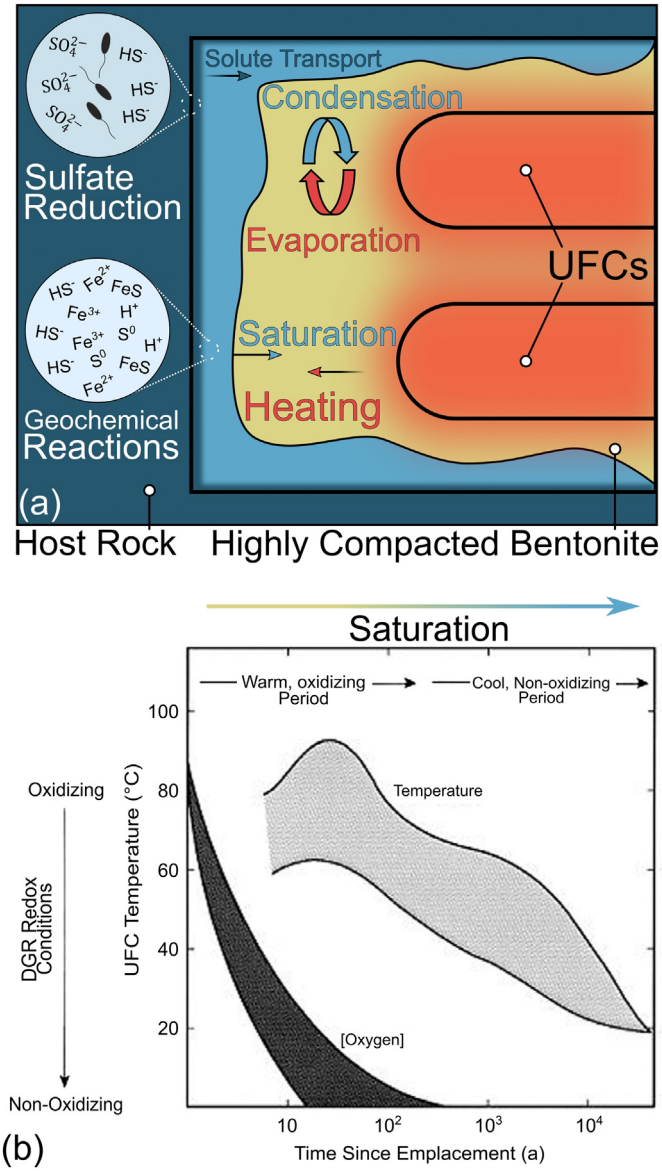

Fig. 1. (a) Key DGR processes driving HS^- production, consumption, and transport and (b) the expected evolution of DGR environmental conditions (adapted from King et al. (2008) with permission of Elsevier).

Specific to HS^- corrosion, Briggs et al. (2017b) developed a multi-dimensional chemical transport model that used the most up-to-date design information from the NWMO to model HS^- transport in the proposed Canadian DGR. This model has been used to understand issues like: (*i*) geometry effects causing higher corrosion rates around the UFC end-caps, (*ii*) the ultimate corrosion depth over one million years, and (*iii*) the influence of preferential pathways (Briggs and Krol, 2018; Briggs et al., 2017a; Briggs et al., 2017b). While these studies have elucidated many aspects of HS^- transport in the DGR, not all processes have been coupled (e.g., multiphase flow movement, mechanical effects, geochemical reactions, biological processes), and it is not clear which processes need to be included to reliably forecast the overall extent of MIC.

This study identifies which coupled processes govern HS^- transport through the DGR by presenting the results and novel insights from numerically modelling HS^- transport through the bentonite buffer in the proposed Canadian DGR. This 3D model couples thermal, hydraulic, and chemical transport processes and considers sensitivities in crystalline and sedimentary host rocks undergoing heating (due to the radioactive decay of the used nuclear fuel) and saturation (due to wetting from the surrounding host rock). Altogether, this study reveals how these processes influence HS^- transport and provides valuable guidance on which others are critical in understanding the long-term risks posed by HS^- corrosion.

2. Methodology

2.1. Governing equations

The model was developed in COMSOL 5.6 Multiphysics (COMSOL, 2021), a commercial finite-element analysis tool, chosen because of its reliability due to monitored commercial releases and verification procedures. All numerical model calculations in were performed via COMSOL. The thermal, hydraulic, and chemical (THC) coupled model developed in this study combined the effects of saturation, heat production, and chemical transport in a 3D domain. All key simulations performed for this study are detailed in Table 1 and extra model information is presented in the Supplementary Materials, Table S.1.

The infiltration process was simulated using Richard's equation to model the capillary pressure-saturation relationship and neglected the dynamics in the air phase (i.e., gas movement in the subsurface) (Bear, 1972):

$$\left(C_m + S_e S_y\right)\frac{\partial H_p}{\partial t} = \nabla\left(\frac{k_r k \rho_w g}{\mu_w}\nabla\left(H_p + z\right)\right) \tag{2}$$

C_m is the specific moisture capacity, S_e is the effective saturation of the bentonite that normalizes the saturation (S) to the full (S_f) and residual (S_r) saturations ($S_e = [S - S_r]/[S_f - S_r]$), S_y is the storage coefficient, H_p is the pressure head ($H_p = p_w/\rho_w g$), k is the intrinsic permeability, ρ_w is the water density, p_w is the water pressure, μ_w is the water viscosity, g is the gravitational constant, z is the elevation head, and k_r is the relative permeability parameter. The constitutive relationships used within Richards' equation to model unsaturated flow followed the formulations from van Genuchten (1980):

$$\begin{aligned}
S &= \begin{cases} S_r + S_e\left(S_f - S_r\right) & H_p < 0\,\mathrm{m} \\ S_f & H_p \geq 0\,\mathrm{m} \end{cases} \\
S_e &= \begin{cases} \dfrac{1}{\left(1 + \left|\alpha H_p\right|^n\right)^m} & H_p < 0\,\mathrm{m} \\ 1 & H_p \geq 0\,\mathrm{m} \end{cases} \\
C_m &= \begin{cases} \dfrac{\alpha m}{1-m}\left(\phi S - \phi S_r\right)S_e^{\frac{1}{m}}\left(1 - S_e^{\frac{1}{m}}\right)^m & H_p < 0\,\mathrm{m} \\ 0 & H_p \geq 0\,\mathrm{m} \end{cases} \\
k_r &= \begin{cases} S_e^{0.5}\left(1 - \left[1 - S_e^{\frac{1}{m}}\right]^m\right)^2 & H_p < 0\,\mathrm{m} \\ 1 & H_p \geq 0\,\mathrm{m} \end{cases}
\end{aligned} \tag{3}$$

Table 1
Key numerical simulations (see additional details and references in the Supplementary Materials, Table S.1).

Run #	Physics simulated[a]	Host rock type	Bentonite permeability k_b [m^2]	Host rock permeability[b] k_{crys}, k_{sed} [m^2]	Initial bentonite saturation S_0 [%]
1	C	Crystalline	6E-21	4E-17	67
2	HC	Crystalline	6E-21	4E-17	67
3	TC	Crystalline	6E-21	4E-17	67
4	THC	Crystalline	6E-21	4E-17	67
5	THC	Crystalline	6E-21	4E-18	67
6	THC	Crystalline	6E-21	4E-19	67
7	THC	Crystalline	6E-21	4E-20	67
8	THC	Crystalline	6E-21	4E-21	67
9	THC	Crystalline	6E-21	4E-22	67
10	THC	Crystalline	6E-21	4E-23	67
11	THC	Crystalline	6E-21	4E-17	45
12	THC	Crystalline	6E-21	4E-17	89
13	C	Sedimentary	1E-19	2E-21 (k_h), 2E-22 (k_v)	67
14	HC	Sedimentary	1E-19	2E-21 (k_h), 2E-22 (k_v)	67
15	TC	Sedimentary	1E-19	2E-21 (k_h), 2E-22 (k_v)	67
16	THC	Sedimentary	1E-19	2E-21 (k_h), 2E-22 (k_v)	67
17	THC	Sedimentary	1E-19	2E-22 (k_h), 2E-22 (k_v)	67
18	THC	Sedimentary	1E-19	2E-20 (k_h), 2E-22 (k_v)	67
19	THC	Sedimentary	1E-19	2E-21 (k_h), 2E-22 (k_v)	45
20	THC	Sedimentary	1E-19	2E-21 (k_h), 2E-22 (k_v)	89

[a] Using the Chemical (C), Hydraulic (H), and Thermal (T) multi-physics combinations.

[b] Isotropic (k_{crys}) and horizontal ($k_{h,sed}$) permeabilities were varied in the crystalline and sedimentary models, respectively. Base cases, corresponding to the current Canadian DGR design, for sedimentary and crystalline models are highlighted. The differences in sedimentary and crystalline bentonite permeabilities were assumed due to the differences in groundwater salinity, where the total dissolved solids are anticipated to be 0.5–60 and 20–400 g L^{-1} in the crystalline and sedimentary host rock, respectively (Duro et al., 2010).

where ϕ is the porosity, and α, n, and m are constant properties inherent to the soil and are given in the Supplementary Material, Table S.1 (note that $m = 1 - 1/n$).

The energy transport was modelled with a local thermal equilibrium model, i.e., all phases (liquid, solid, and gas) were assumed to be the same temperature locally:

$$\rho C_{p_{eff}} \frac{\partial T}{\partial t} = \nabla\left(\lambda_{eff} \nabla T\right) + q \tag{4}$$

where T is temperature, ρC_{peff} is the effective heat capacity per unit volume, λ_{eff} is the effective thermal conductivity, and q is a volumetric source term. The effective thermophysical properties (ρC_{peff} and λ_{eff}) were estimated as volume-weighted arithmetic means (Nield and Bejan, 2013):

$$\begin{aligned} \rho C_{p_{eff}} &= \phi S \rho_w C_{p_w} + (1-\phi)\rho_s C_{p_s} + \phi(1-S)\rho_g C_{p_g} \\ \lambda_{eff} &= \phi S \lambda_w + (1-\phi)\lambda_s + \phi(1-S)\lambda_g \end{aligned} \tag{5}$$

where the subscripts s, w and g note the solid (i.e., bentonite and host rock), liquid (i.e., groundwater), and gas (i.e., air) phases, respectively. All water and air thermophysical properties were functions of temperature following standard empirical results embedded within COMSOL's material library (COMSOL, 2021), and the solid properties were assumed constant (see Supplementary Materials, Table S.1). HS^- species transport was assumed to be unreactive and diffusion-controlled, and was modelled as:

$$\phi \frac{\partial C}{\partial t} + C C_m \frac{\partial H_p}{\partial t} = D_e \nabla^2 C \tag{6}$$

where C is the HS^- concentration, D_e is the effective HS^- diffusion coefficient. The diffusivity was estimated from the saturation, porewater diffusion coefficient (D_o), diffusion-accessible porosity (ϕ_e), and tortuosity (τ) following (Shackelford and Moore, 2013):

$$\begin{aligned} D_e &= S \frac{\phi_e}{\tau} D_o \\ \tau &= \left(\frac{L_e}{L}\right)^2 \end{aligned} \tag{7}$$

where L and L_e are the straight-line and actual travel distances in the porous medium. HS^- diffusion in bentonite is anticipated to be complicated by many factors, e.g., geochemical reactions/sorption, anion exclusion effect (which lowers the diffusion accessible porosity of anionic species and can lead to semipermeable membrane behaviour), and the influence of surface and/or interlayer diffusion (Chowdhury et al., in press-a; Shackelford and Moore, 2013). Many of these processes were not modelled explicitly because they depend on both bentonite conditions and groundwater chemistry and there are few estimates of HS^- diffusivity through bentonite (Eriksen and Jacobsson, 1982; Pedersen et al., 2017). Therefore, HS^- was assumed to be unaffected by sorption/geochemical processes (i.e., to provide a conservatively high estimate of HS^- transport rates) and ϕ_e/τ reduced the D_0 value (assumed as 10E-9 m^2 s^{-1} (SKB, 2010)) by 0.01, thereby leading to an ambient D_e = 10E-11 m^2 s^{-1}. This approach is consistent with Briggs et al. (2017b) and aligns with the limited D_e measurements of HS^- through bentonite (Pedersen et al., 2017) and other unreactive anions (e.g., Cl^-) (Van Loon et al., 2007; Van Loon et al., 2003).

The temperature influence on D_e was assumed to be proportional to the changes in temperature and viscosity following (Einstein, 1905; King et al., 2017b):

$$\frac{D_{o,T1}}{D_{o,T2}} = \frac{T_1}{T_2} \frac{\mu_{w,T2}}{\mu_{w,T1}}. \tag{8}$$

The advective terms were neglected in Eqs. (4) and (6) as Darcy velocities were extremely slow due the low bentonite permeabilities. The maximum Peclet numbers in the chemical-transport and thermal models were calculated as $Pe_C = v_D d_p/\phi D_e$ = 2E-4 and $Pe_T = v_D d_p \rho C_{peff}/\phi\lambda_{eff}$ = 5E-9, respectively, under the most conservative conditions, i.e., with (*i*) the highest modelled seepage velocity (v_D/ϕ = 5E-8 m s^{-1} from the base crystalline case – Run #4, Table 1), (*ii*) the average pore diameter of bentonite (d_p = 3E-8 m) (Dixon, 2019) as the diffusion length, and (*iii*) the lowest mass and thermal diffusivities in the crystalline rock at ambient temperatures (D_e = 1E-11 m^2 s^{-1} and $\lambda_{eff}/\rho C_{peff}$ = 3E-7 m^2 s^{-1}). These extremely low Peclet numbers (<<1) indicate that the diffusive processes dominated mass and energy transport; therefore, advective transport was safely neglected (Kaviany, 1995). In addition, a confirmation simulation was performed under the most conservative case assuming that advection was not negligible, and results were practically identical to the same simulation with advection neglected (see additional details in the Supplementary Materials, Section S.1 and Fig. S.1).

To approximate the effect of HS^- transport on container integrity, a conservative estimate of the HS^- corrosion rate (dx/dt_{corr}) was calculated assuming that surface reactions proceeded much faster than the HS^- transport, i.e., that the corrosion was limited by HS^- transport to the UFC (King et al., 2017a):

$$\frac{dx}{dt_{corr}} = \frac{\dot{N}''_{HS} f_{HS} M_{Cu}}{\rho_{Cu}} \tag{9}$$

where $\dot{N}''_{HS}$ is the molar flux of HS^- to the UFC surface, f_{HS} is the stochiometric factor (i.e., 2 from Eq. (1)), M_{Cu} is the molar mass of copper (Cu), and ρ_{Cu} is the density of copper.

2.2. Modelling domain

Fig. 2 presents the model domain and boundary conditions. The model was used to simulate the THC dynamics around two UFCs located 500 m below ground surface surrounded by highly compacted bentonite in a host rock (either crystalline or sedimentary), which reflects the NWMO design, anticipated site-conditions, and builds upon previous DGR numerical modelling efforts (Briggs and Krol, 2018; Guo, 2017). As shown in Fig. 2, the mesh was most refined near the UFCs to capture HS^- transport near the containers throughout time and was coarser away from the UFCs for computational efficiency. A mesh convergence study was performed that showed a minimum mesh size of 0.01 m near the UFCs led to reliable results (see convergence plots in the Supplementary Materials, Fig. S.2).

The heat generation from the UFCs was modelled using volumetric heat source terms following Tait et al. (2000). The domain stretched from the surface (0 m) down to 10,000 m below into the host rock. The top surfaces assumed constant temperature boundary conditions equal to the average surface temperature expected at the DGR location, i.e., 5 and 10 °C in the crystalline and sedimentary models, respectively. The bottom surfaces also assumed constant temperatures of 125 °C (crystalline) and 113 °C (sedimentary), due to geothermal gradients of 0.0120 °C m^{-1} (crystalline) and 0.0103 °C m^{-1} (sedimentary), respectively (Guo, 2016; Guo, 2018). The initial temperature conditions in the sedimentary model therefore did not account for anticipated rock layers, which are expected to yield slightly different thermal gradients (Guo, 2018). However, this layering is not anticipated to strongly affect the trends investigated in this study, and were therefore not modelled for computational efficiency. Note that, due to the increasing hydrostatic pressures downward, the water is expected to remain in the liquid phase throughout the host rocks. The 10,000 m model domain depth was chosen such that the bottom boundary was far enough from the UFCs that it would not artificially influence the temperature distribution over the long modelling times considered (i.e., 1,000,000 years). The order of magnitude of this domain depth constraint can be shown from a scale analysis ($x_c \sim \sqrt{\lambda_{eff}/\rho C_{p\,eff} t_c}$), where x_c is the characteristic distance that affects the temperature distribution after a characteristic time (t_c) (Nield and Bejan, 2013). Adiabatic boundary conditions were applied around the perimeter of the domain, which cut through symmetrical sections of the UFCs, to simulate an infinite tabular array rooms (following Guo (2016)). These boundaries led to a false second peak in the temperature histories that Guo (2017) explored in detail. This false peak was not corrected for in this study as it did not strongly affect the key trends investigated.

Constant hydraulic heads were assumed at all boundaries of the model domain and the bentonite was assumed to be initially water-saturated at 67% (Gobien et al., 2018) and the host rock was assumed fully saturated and constant. Because the footprint of the region modelled was small (7.5 and 11 m^2 in the crystalline and sedimentary models, respectively), these constant hydraulic heads were assumed to be reasonable due to the small groundwater gradient expected across the placement site. In addition, the surrounding host rock was assumed to be fully saturated throughout time due to the high capillary pressure required for air to enter the host rock (NWMO, 2011); therefore, the description of flow movement throughout the host rock reduced to the standard transient equation in fully saturated porous media (i.e., $H_p \geq 0$ m, $k_r = S_e = 1$, and $C_m = 0$ in Eqs. (2) and (3)).

Constant HS^- concentrations of 1 and 0 ppm (g m^{-3}) were assumed at the host rock-bentonite interface (from sulfate-reducing bacteria) and UFCs' surfaces (from corrosion reactions), respectively. This HS^- boundary condition at the host rock-bentonite interface is conservative, as the HS^- concentration in the Canadian shield is anticipated to be near 30–100 ppb (Briggs et al., 2017b; Hall et al., 2021). Though the HS^- formed by sulfate-reducing bacteria would also diffuse away from the DGR through

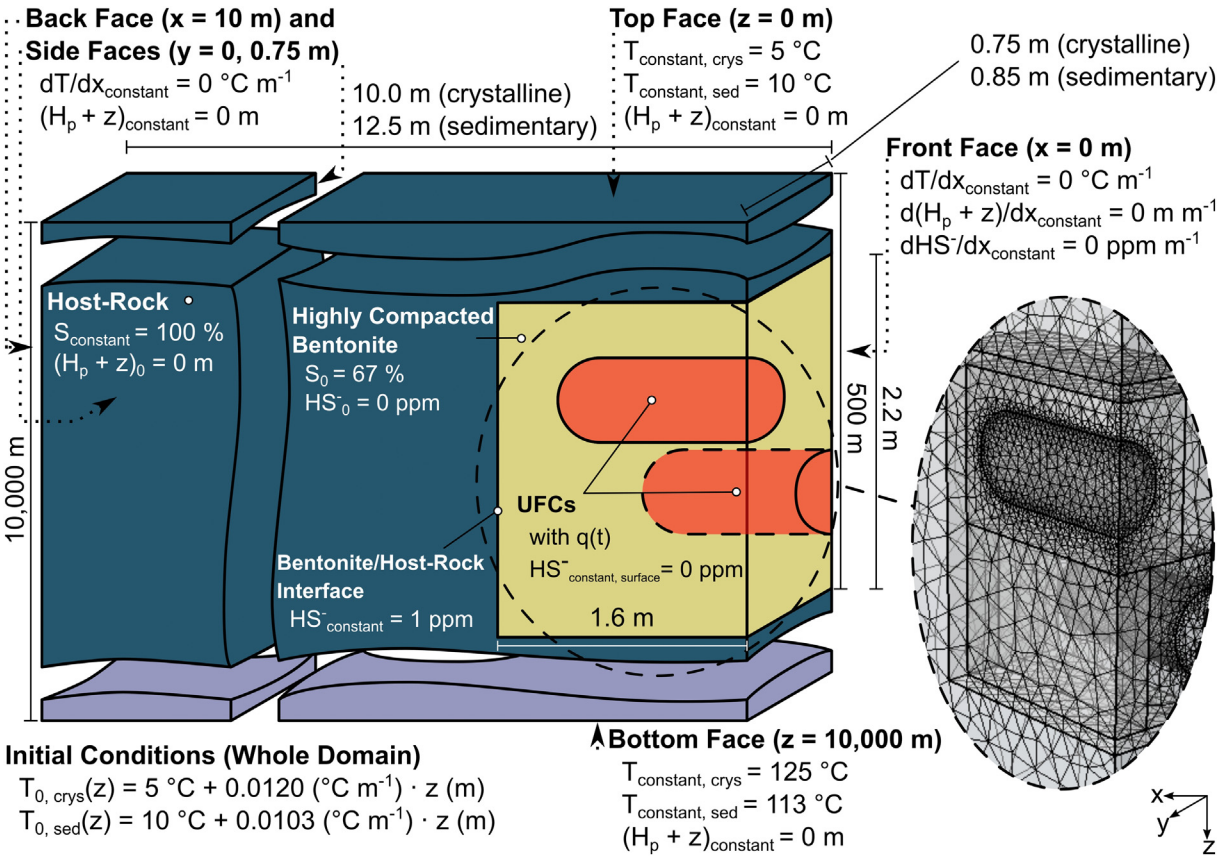

Fig. 2. Model geometry showing the key sections: (*i*) host rock (either crystalline or sedimentary), (*ii*) highly compacted bentonite, and (*iii*) used fuel containers (UFCs). The call-out circle shows a screenshot of the model domain mesh near the UFCs.

the host rock, these dynamics are not expected to affect HS^- corrosion, and were therefore neglected for computational efficiency.

3. Results and discussion

3.1. Exploring key sensitivities to host rock and bentonite properties

The THC model was used to investigate the sensitivity of host rock and bentonite parameters on key DGR variables (i.e., temperature, effective saturation, and HS^- flux) throughout time and space. Figure 3 illustrates the sensitivities due to initial bentonite saturation (S_0) and host rock permeabilities, i.e., the isotropic (k_{crys}) and horizontal ($k_{h,sed}$) permeabilities in the crystalline and sedimentary models (keeping $k_{v,sed}$ constant), respectively (see Table 1).

The average DGR effective saturation profiles (Fig. 3a-b) align with expectations. That is, the degree of saturation increased as water flowed in from the surrounding saturated host rock and filled the bentonite pore spaces. As expected, the saturation behaviour was sensitive to the host rock permeability and initial bentonite saturation, where the saturation time increased with decreasing permeabilities and initial degrees of saturation. At an initial saturation (S_0) of 67%, the crystalline model reached 100% saturation within 20 to 80 years when the host rock permeability (k_{crys}) ranged from 4E-17 to 4E-21 m^2, respectively. When the initial saturation was 89% and 45% (k_{crys} = 4E-17 m^2), the crystalline model saturated within 10 and 30 years, respectively, showing that the effect of k_{crys} was greater than that of S_0. On the other hand, the sedimentary model (S_0 = 67%) assumed lower rock permeabilities and took 35 to 720 years to fully saturate with $k_{h,sed}$ = 2E-20 to 2E-22 m^2, respectively, and 105 to 205 years when S_0 = 89 to 45% ($k_{h,sed}$ = 2E-21 m^2), respectively. This range of saturation times, i.e., between 10s and 100s of years, agrees well with other DGR studies (Birkholzer et al., 2019; Jing and Nguyen, 2005; Millard et al., 2004). When the crystalline host rock permeabilities were higher than the bentonite permeability ($k_{b,crys}$ = 6E-21 m^2), the saturation time became insensitive to the host rock permeability. This is expected because the bentonite permeability limited the rate of saturation in relatively high-permeability host rock simulations. This result highlights a valuable practical point: the DGR selection site (and associated host rock characteristics) can play an important role in delaying saturation, but it will not severely expedite the saturation. In fact, the bentonite characteristics would limit the saturation evolution in host rocks with a high permeability, e.g., due to fractures, perhaps within the excavated damage zone (Perras and Diederichs, 2016).

Though the bentonite permeability and swelling relationships with saturation were not explicitly modelled in this study, it is valuable to highlight how these dynamics would alter the saturation behaviour. At the beginning of saturation, the outer region of the bentonite hydrates first and starts to swell and consequently its dry density is decreased. The swelling bentonite will compress the adjacent regions (towards inner, drier regions) and therefore increase the dry density of the inner regions. In turn, the adjacent inner regions start to swell and compress the outer regions, resulting in increasing the dry density of the outer regions. As a result of this process, the outer regions can be denser and consequently its permeability can be reduced. In other words, even less groundwater can be available as the permeability can be lowered throughout saturation (Kim, 2017).

The average UFC temperature profiles in Fig. 3c-d also agree with expectations. That is, the UFC surface temperature increased initially due to used nuclear fuel thermal decay (Tait et al., 2000). This decay caused the UFC surface to heat up to ~80 °C after 50 and 40 years in the crystalline and sedimentary models, respectively, which agrees with similar modelling studies (Briggs and Krol, 2018; Guo, 2017; King et al., 2017b; King et al., 2008). In particular, the close agreement with Guo (2016) serves as robust verification, which bolsters confidence in the model assumptions and implementation (see Supplementary Materials, Fig. S.4). The second temperature peak is also common in similar DGR studies, which is an artefact due to the near-field adiabatic boundary condition (Guo, 2017). Fig. 3c-d also show that the temperatures were minimally affected by varying the host rock permeability and initial bentonite saturation. This minimal sensitivity was due to numerous factors, e.g., (*i*) heat transfer was driven by conduction and convective heat transport was neglected, as the small Darcy fluxes facilitated very small Peclet numbers (<<1, as discussed above); and (*ii*) because the thermophysical properties were not very sensitive to saturation changes (further discussed below).

Fig. 4a and b presents snapshots of the predicted saturations throughout space at selected times in the base case crystalline (Run #4) and sedimentary (Run #16) models, respectively (see Table 1). These snapshots are taken from the Supplementary video provided. Fig. 4c-d show snapshots

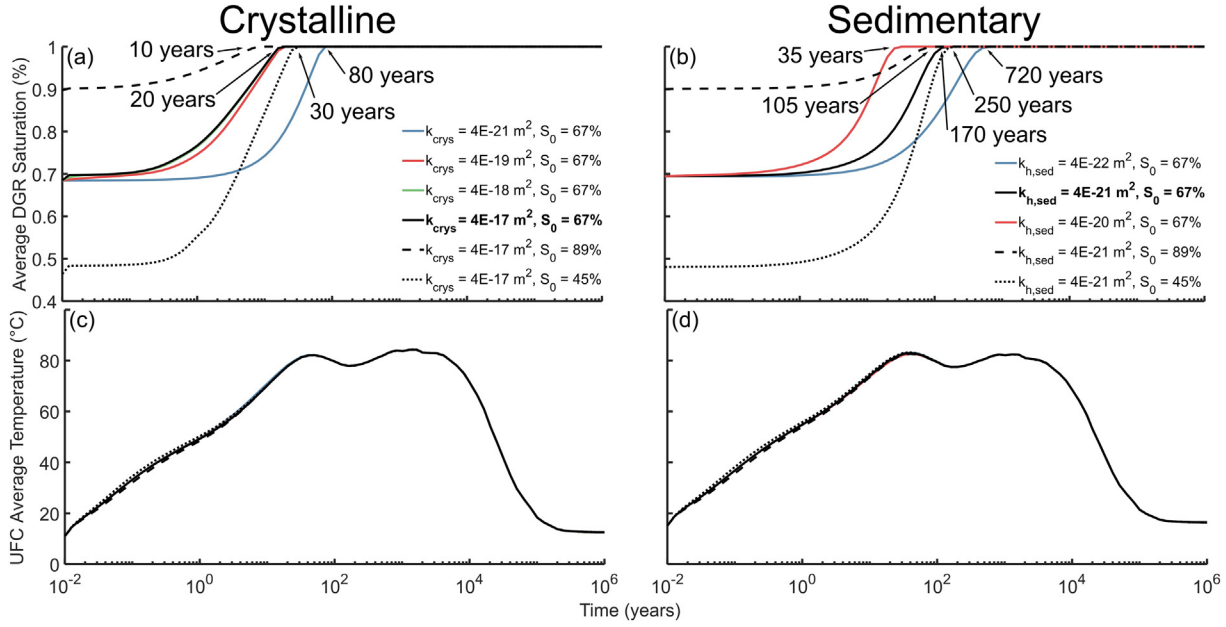

Fig. 3. The simulated evolutions of: (a, b) average DGR effective saturation and (c, d) average UFC surface temperature over the design life of the DGR from varying the initial saturation, isotropic rock permeabilities (in the crystalline model in frames a and c), and horizontal rock permeabilities (in the sedimentary model in frames b and d). The base case scenarios are bolded.

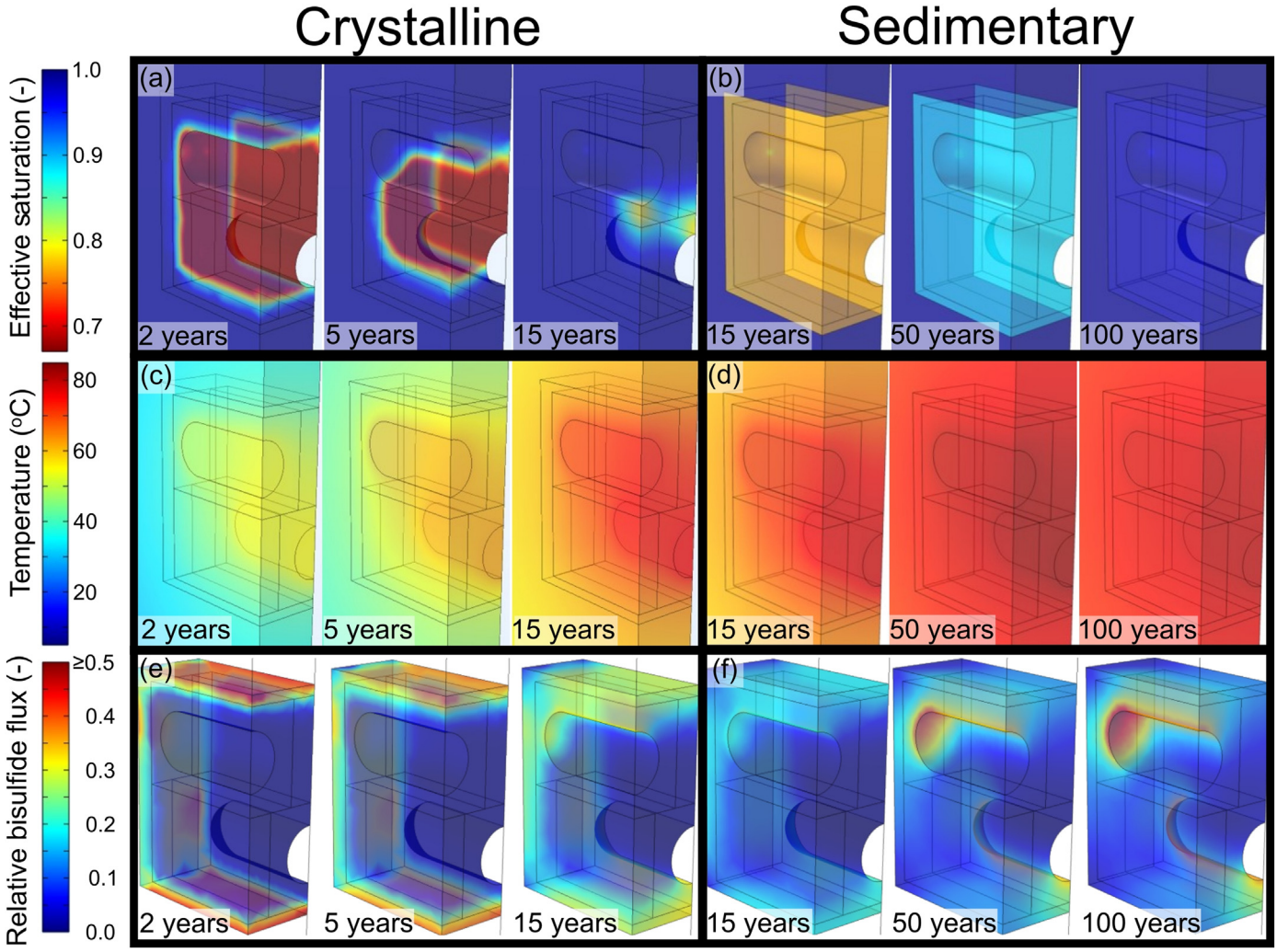

Fig. 4. The simulated spatial distributions of the: (a, b) effective saturation, (c, d) temperature, and (e, f) relative HS^- flux from the base case (a, c, e) crystalline and (b, d, f) sedimentary models (see Table 1 for the base case conditions).

of the domain temperatures under the same conditions as Fig. 4a-b, respectively. Fig. 4e-f show the HS^- flux distribution, which was influenced by both the saturation and temperature changes (see Eqs. (7) and (8)).

Insights into the processes driving these saturation differences in crystalline and sedimentary models can be seen in Fig. 4a-b. The crystalline model exhibited a sharp wetting front that fully saturated the outer edges of the domain and moved inwards (Fig. 4a). However, this sharp wetting front is not seen in the sedimentary model (Fig. 4b). Instead, these snapshots show that the bentonite saturation in the sedimentary model increased nearly uniformly. These different saturation behaviours are due to the differences in host rock and bentonite permeabilities assumed between the crystalline and sedimentary models, which are further explored below in Fig. 5.

The spatial evolution of heat generated from the UFCs (Fig. 4c-d) shows characteristic diffusive transport of energy away from the UFCs in the crystalline and sedimentary models, respectively, which were only minimally influenced by the saturation changes. As mentioned above, this insensitivity was partly because the effective thermophysical properties in the

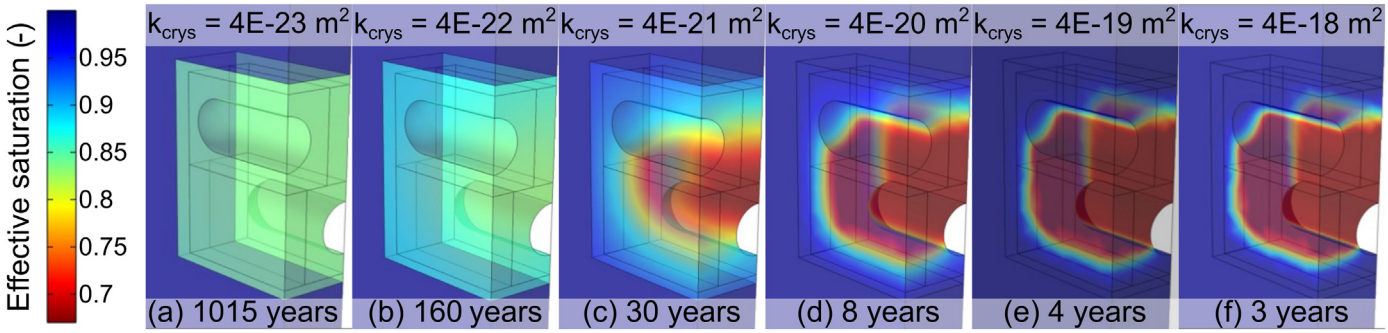

Fig. 5. Wetting front distribution when the crystalline DGR is half-saturated from 67 to 100% (i.e., S_{avg} = 85%) assuming different host rock (k_{crys}) permeabilities (Runs #4–10) and noting the times when half-saturation occurred. The bentonite permeability ($k_{b,crys}$) was 6E-21 m^2 in all simulations.

crystalline and sedimentary models (primarily λ_{eff} and ρC_{peff}) did not vary strongly with saturation from 45 to 100% (see Supplementary Materials, Fig. S.3).

Fig. 4e-f visualizes the HS^- flux throughout space, which was influenced by both temperature and saturation (see Eqs. (6)–(8)). Because HS^- was assumed to only transport in the water phase, the effective diffusion coefficient (D_e) scaled linearly with saturation (see Eq. (7)). Therefore, the HS^- flux distribution in Fig. 4e-f was generally highest in the most saturated regions, and the saturation behaviour influenced the non-uniformity of the HS^- flux. This relationship is best seen by comparing the saturation front in the crystalline model (Fig. 4a) with the resulting HS^- flux distributions in Fig. 4e, where the HS^- flux patterns generally followed the wetting front. These results highlight how the unsaturated regions restrict HS^- transport and thereby delays HS^- corrosion. Furthermore, after saturation (which is best seen after 100 years in Fig. 4f), the highest HS^- flux occurred at the end-caps of the UFC due to their hemispherical geometry (Briggs et al., 2017b). These high fluxes around the end-caps are also seen in the crystalline model after sufficiently long-times (>100 years; see the Supplementary Materials, Fig. S.5). The temperature evolution in the DGR also had a strong influence on the HS^- flux, as D_e was assumed to scale with temperature (see Eq. (8)). The implications of this relationship are shown in Figs. 6 and 7 and discussed below.

Altogether, Fig. 4 highlights how the temperature and saturation evolutions affect HS^- transport throughout space at snapshots in time. While the average DGR saturation (Fig. 3a-b) and UFC temperature profiles (Fig. 3c-d) examine their evolutions throughout the entire anticipated DGR lifespan (i.e., 1,000,000 years), the snapshots in Fig. 4 only highlight their implications during early-times, i.e., the first 100s of years. The impact of temperature and saturation evolutions on HS^- transport is dominant during these early-times.

Fig. 5 further explores the effect of the host rock (crystalline) permeability on the wetting front dynamics. This figure shows that the differences between the host rock and bentonite permeabilities govern the saturation behaviour. Fig. 5a shows that when the host rock permeability (k_{crys} = 4E-23 m^2) was much lower than bentonite permeability ($k_{b,crys}$ = 6E-21 m^2) the saturation was nearly uniform throughout space (i.e., similar to Fig. 4b). However, when the host rock permeability was increased to the same order as the bentonite permeability (k_{crys} = 4E-21 m^2 in Fig. 5c), the wetting front became better defined with sharp saturation differences over a thin region (i.e., similar to Fig. 4a).

The differences in the saturation behaviour between the crystalline and sedimentary models were due to the assumed host rock and bentonite permeabilities. Compared to the crystalline model, the sedimentary model had a lower host rock permeability as it is assumed that sedimentary rock will contain fewer fractures than crystalline (NWMO, 2011). Furthermore, a lower bentonite permeability was used in the crystalline model as its groundwater is anticipated to be less saline than the sedimentary groundwater. Higher salinity would reduce bentonite double layer swelling and result in a higher permeability (Dixon, 2019; Dixon et al., 2018; NWMO, 2011). Therefore, the sedimentary host rock (k_{sed} = 2E-22 to 2E-20 m^2) was much less permeable than its bentonite ($k_{b,sed}$ = 1E-19 m^2), which limited the groundwater transport rate into the sedimentary DGR. This groundwater transport limitation stretched the saturation distribution over a larger region in the sedimentary model than the crystalline model. In other words, the saturation differences dissipated in the sedimentary bentonite faster than water entered, which led to a dull wetting front shape (Fig. 4b) as opposed to the sharp wetting front shape in the crystalline bentonite (Fig. 4a).

3.2. Exploring key sensitivities to governing physics

Fig. 6 visualizes the evolution of HS^- flux at the centre of the upper UFC end-caps normalized to the maximum flux observed in the crystalline and sedimentary models (i.e., Runs #1–4 and #13–16, respectively, Table 1). In these runs, all parameters were kept the same but the influence of the thermal (T) and hydraulic (H) processes on chemical transport (C) throughout 1,000,000 years. The centre of the UFC end-caps were chosen to present the HS^- flux evolution as they are most susceptible to HS^- corrosion due to their geometry (Briggs and Krol, 2018; Briggs et al.,

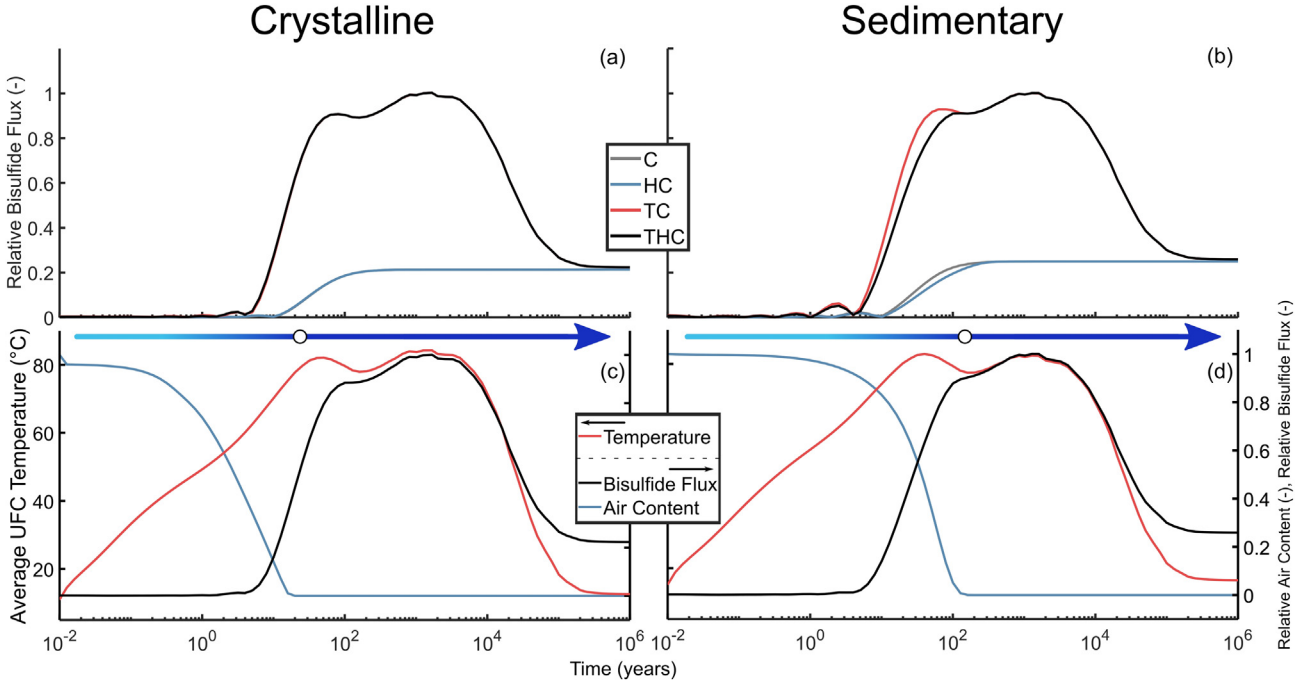

Fig. 6. Relative bisulfide fluxes estimated at UFC surface (upper end-caps) in (a) crystalline and (b) sedimentary DGR models under different modelling assumptions: chemical transport-only (C); chemical transport coupled with saturation changes (HC); chemical transport coupled with thermal changes (TC); and chemical transport coupled with both thermal and saturation changes (THC). The average UFC surface temperature and relative DGR air content evolutions from the THC models are overlain with the normalized corrosion histories in the (c) crystalline and (d) sedimentary models. The colour gradient arrows note the progression of DGR saturation, where the overlain circle approximately indicates the time to full saturation.

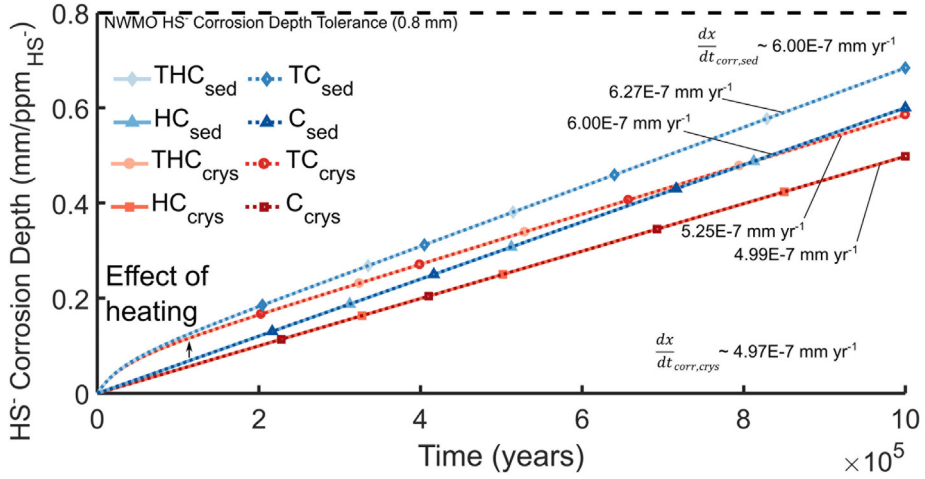

Fig. 7. Modelled HS^- corrosion depths calculated using different modelling assumptions (i.e., C, HC, TC, and THC) in either the crystalline or sedimentary domains and plotted on a linear time scale. The slopes are from linear regression analyses performed on each dataset from 200,000 to 1,000,000 years.

2017b). In addition, the upper end-caps experienced slightly more HS^- corrosion due to a larger contribution region because of the DGR layout (see Supplementary Materials for a comparison between the HS^- fluxes at the upper and lower end-caps, Section S.2). As such, the HS^- flux histories in Fig. 6 were taken at the upper UFC end-caps.

Fig. 6a and b presents the normalized fluxes in the crystalline and sedimentary models, respectively. By comparing various model couplings (i.e., C, HC, TC, and THC using the base case conditions, Table 1), the influence of each process on HS^- transport can be untangled. Fig. 6c and d overlays the normalized THC HS^- fluxes in the crystalline and sedimentary models, respectively, with the average UFC surface temperature and relative DGR air content results (derived from results in Fig. 3).

The result from the C model in Fig. 6 shows the relative HS^- fluxes in an ambient temperature, fully saturated system. The C results align very well with theoretical results and further verify that the model is properly developed (see a comparison with an analytical model in the Supplementary Materials, Section S.2). The differences between the crystalline and sedimentary C model results are due to assuming (*i*) a higher ambient temperature driving faster diffusion in the sedimentary model (15 °C) than the crystalline model (11 °C) (see Eq. (8)) and (*ii*) different lateral UFC spacings (see Supplementary Materials for quantified UFC spacings, Fig. S.7). These differences are further explored below in Fig. 7.

By coupling the hydraulic process with HS^- transport at ambient temperatures (HC), the onset of HS^- flux at the end-caps was delayed (which was most pronounced in the sedimentary model in Fig. 6b). As discussed above, this delay was because HS^- was assumed to transport in the liquid phase and was therefore restricted through partially saturated bentonite. However, once saturated (i.e., after 20 and 170 years in the crystalline and sedimentary models, respectively), the HS^- fluxes matched those from the C model.

When coupling temperature changes with HS^- transport in a fully saturated system (TC), the HS^- flux profile exhibited a similar shape as the temperature profiles presented above in Fig. 3c-d, and further discussed below in Fig. 6c-d. This matching is due to the temperature dependence assumed in the molecular diffusion coefficient, D_o (see Eq. (8)). Therefore, as the temperature throughout the DGR increased, so did D_o, which led to faster diffusion during UFC heating.

Coupling all processes together (THC) shows the overall influence of saturation and heating on HS^- flux. That is, saturation delayed the arrival of HS^- like in the HC model but, once fully saturated, the HS^- fluxes then matched those observed in the TC model. The average DGR air content (calculated as $(1 - S_e)_{avg}/(1 - S_{e,0})_{avg}$ to highlight the saturation dynamics) and average UFC surface temperatures are overlain on Fig. 6c and d to illustrate how their trends impact HS^- flux. These figures show the matching between the average UFC surface temperature and the HS^- fluxes, and the delayed onset due to saturation (i.e., full saturation occurs when the average relative air content approaches 0). Compared to Fig. 1b (i.e., the expected evolution of key parameters affecting UFC corrosion), the temperature and air content qualitatively follow the anticipated temperature and oxygen content evolutions in the DGR, respectively. This comparison further confirms that this model is reproducing the key trends anticipated in the DGR, and their influence on HS^- transport. Altogether, Fig. 6 highlights how UFC heating and bentonite saturation affect the HS^- transport to the UFC end-caps, and therefore impact corrosion rates. That is, UFC heating accelerates HS^- corrosion through increasing its rate of transport, but the bentonite saturation process delays the onset of HS^- corrosion.

3.3. Exploring influence of various physics on HS^- corrosion depth

The primary motivator of understanding HS^- transport through the DGR is to develop accurate predictions of microbiologically-influenced corrosion on the UFC. Fig. 7 uses the flux results in Fig. 6 to estimate HS^- corrosion depth per ppm of HS^- over the lifespan of the DGR. These corrosion estimates integrate the HS^- flux at the upper UFC end-cap centre over time to estimate the evolution in HS^- corrosion depth following Eq. (9). This figure is expressed per ppm HS^-, as the corrosion depth scales with the HS^- concentration at the host rock-bentonite interface, which is currently unknown. Altogether, this figure emphasizes the overall influence of both heating and saturation on the HS^- corrosion depth.

Unlike Figs. 3 and 6, which focus on the HS^- flux results over the early-times due to the logarithmic time-scale, the linear scale in Fig. 7 clearly illustrates the impact of different processes on the HS^- corrosion. These results show that many of the differences between the C, HC, TC, and THC models were due to the transient effects that occurred over a relatively short period (i.e., particularly UFC heating over the first 10,000s of years). While these differences are important to understand for other reasons, e.g., in forecasting oxic corrosion processes (Hall et al., 2021), Fig. 7 illustrates that they do not strongly influence HS^- corrosion. That is, the THC and HC results nearly perfectly overlay the TC and C results, respectively. This indicates that the delay due to saturation barely impacts the HS^- corrosion depth (<1%). Conversely, UFC heating does have a noticeable effect, but the effect is small; UFC heating increased HS^- corrosion by 14% and 18% after 1,000,000 years in the crystalline and sedimentary models, respectively.

Towards understanding the key terms driving the trends in Fig. 7, the HS^- corrosion rate (dx/dt_{corr}) in Eq. (9) was approximated assuming that HS^- flux at the UFC at the end-caps was equal to linear diffusion from the host rock-bentonite interface ($\dot{N}_{HS} \approx \tilde{D}_{e,0} C_0 / x_f$). In addition, a

dimensionless geometry factor (A_f) was included to account for the multi-dimensional contribution of HS^- flux onto the end-caps, which is not considered in Eq. (9). See additional details in the Supplementary Materials, Section S.2.

$$\frac{dx}{dt_{corr}} \sim A_f \frac{D_{e,0} C_0 f_{HS} M_{Cu}}{x_f \rho_{Cu}}. \quad (10)$$

Compared to the minimal influence from UFC heating and bentonite saturation, Fig. 7 shows that the terms in Eq. (10) govern the HS^- corrosion rates (i.e., the slopes of all lines). That is, the corrosion rates are closely estimated by populating Eq. (10) with DGR design parameters, including: (*i*) A_f, which accounts for geometry effects and is governed by UFC spacing (see Supplementary Materials, Section S.2); (*ii*) the distance from the end-caps to the bentonite-host rock interface (x_f); (*iii*) the HS^- concentration at the interface (C_0); and (*iv*) the effective diffusivity of HS^- through bentonite at ambient conditions ($D_{e,0}$). From comparing the corrosion rates at late-times (i.e., slopes between 200,000 and 1,000,000 years), Fig. 7 shows that Eq. (10) approximates the modelled corrosion rates within 6%.

While A_f and x_f are relatively straightforward geometric design parameters, $D_{e,0}$ is challenging to resolve as it is influenced by many characteristics that are specific to the DGR and bentonite used (e.g., temperature, water ionic concentration, geochemical reactions, bentonite density). As mentioned above, there are few reliable estimates of $D_{e,0}$ in the literature for HS^- through bentonite (Eriksen and Jacobsson, 1982; Pedersen et al., 2017), and these estimates may not necessarily reflect the $D_{e,0}$ in the Canadian DGR (Chowdhury et al., in press-b). However, Eq. (10) shows how $D_{e,0}$ governs the corrosion rate. Moreover, the key differences between the sedimentary and crystalline models in Fig. 7 were due to the differences in (*i*) A_f (1.65 and 1.56, respectively, as the UFC spacing was larger in the sedimentary than the crystalline model); and (*ii*) $D_{e,0}$ (9E-12 and 8E-12 $m^2 s^{-1}$, respectively, as the ambient temperature was 5 °C warmer in the sedimentary than the crystalline model). These differences led to proportionally more corrosion in the sedimentary than the crystalline models (17–21%). However, even with these conservative assumptions (e.g., high ambient $D_{e,0}$, no retardation from geochemical reactions/sorption), the corrosion at 1,000,000 years in all models was only 0.5–0.7 mm. As noted previously, the concentration of HS^- used in the current model was 1 ppm, which is the extreme upper concentration limit used in the recent assessment of total corrosion for a Canadian DGR by Hall et al. (2021). In that analysis, the maximum copper corrosion by HS^- was simplistically calculated to be 0.8 mm, compared to the total planned copper coating of 3 mm (Hall et al., 2021). The current result substantiates that the proposed Canadian UFC is robustly designed for HS^- corrosion, while accounting for more complicated dynamics.

4. Conclusions

Valuable insight was achieved from rigorous, multi-dimensional modelling that coupled thermal and hydraulic effects on bisulfide (HS^-) transport in the proposed Canadian deep geological repository (DGR) design. This modelling revealed how the thermal output of the used fuel containers (UFCs) could accelerate HS^- transport and the hydraulic effects from low host rock permeabilities and saturation from the surrounding host rock could delay HS^- transport. However, the influence from heating only increased total projected HS^- corrosion by <20% and the influence from saturation had a negligible impact (<1%). Therefore, though these processes lead to important changes during the early-times of the DGR, they do not strongly influence the overall risks posed by HS^- corrosion, which are largely governed by nearly-steady DGR design parameters, including the effective diffusivity of HS^- through bentonite at ambient conditions. Therefore, special focus should be given to these parameters governing diffusion in the DGR, which will be complicated by site conditions (e.g., groundwater geochemistry) and design considerations (e.g., bentonite initial saturation, in-place density, surface chemistry). Future modelling work is underway to account for this information as it becomes available so that the extent of HS^- corrosion can be reliably and accurately predicted.

Supplementary data to this article can be found online at https://doi.org/10.1016/j.scitotenv.2022.153944.

CRediT authorship contribution statement

Tarek L. **Rashwan:** Formal analysis, Investigation, Methodology, Software, Validation, Visualization, Roles/Writing - original draft. **Md Abdullah Asad:** Conceptualization, Data curation, Formal analysis, Investigation, Methodology, Software, Validation, Visualization, Writing - review & editing. **Ian** L. **Molnar:** Conceptualization, Formal analysis, Methodology, Project administration, Resources, Software, Supervision, Writing - review & editing. **Mehran Behazin**: Project administration, Resources, Supervision, Writing - review & editing. **Peter G. Keech**: Project administration, Resources, Supervision, Writing - review & editing. **Magdalena M. Krol:** Conceptualization, Funding acquisition, Methodology, Project administration, Resources, Supervision, Writing - review & editing.

Declaration of competing interest

The authors declare the following financial interests/personal relationships which may be considered as potential competing interests: Peter G. Keech and Mehran Behazin are employed by a company seeking a solution to nuclear waste disposal for Canada. While geological disposal is not a certainty in the company mandate, it is the primary topic of research for Canada as well as nearly all other countries with nuclear energy programs.

Acknowledgements

Funding was provided by the Ontario Research Fund – Research Excellence grant and the Natural Sciences and Engineering Research Council of Canada Collaborative Research and Development Grant in partnership with the Nuclear Waste Management Organization (Toronto, Canada). We acknowledge the additional project support from Sarah Couillard and Iman Roohidehkordi; helpful comments provided by Drs. Ruiping Guo, Scott Briggs, and Chang Seok Kim; and the constructive reviews provided by two anonymous reviewers. We recognize that many Indigenous Nations have longstanding relationships with the territories upon which York University campuses are located that precede the establishment of York University. York University acknowledges its presence on the traditional territory of many Indigenous Nations. The area known as Tkaronto has been care taken by the Anishinabek Nation, the Haudenosaunee Confederacy, and the Huron-Wendat. It is now home to many First Nation, Inuit, and Métis communities. We acknowledge the current treaty holders, the Mississaugas of the Credit First Nation. This territory is subject of the Dish with One Spoon Wampum Belt Covenant, an agreement to peaceably share and care for the Great Lakes region.

References

Ballarini, E., Graupner, B., Bauer, S., 2017. Thermal–hydraulic–mechanical behavior of bentonite and sand-bentonite materials as seal for a nuclear waste repository: numerical simulation of column experiments. Appl. Clay Sci. 135, 289–299.

Baumgartner, P., Tran, T.V., Burgher, R., 1994. Sensitivity analyses for the thermal response of a nuclear fuel waste disposal vault. TR-621, COG-94-258. Atomic Energy of Canada Limited, Chalk River, Canada, p. 40.

Bear, J., 1972. Dynamics of Fluids in Porous Media. Elsevier Publishing Company, Inc., New York.

Bengtsson, A., Pedersen, K., 2016. Microbial sulphate-reducing activity over load pressure and density in water saturated boom clay. Appl. Clay Sci. 132–133, 542–551.

Birkholzer, J.T., Tsang, C.-F., Bond, A.E., Hudson, J.A., Jing, L., Stephansson, O., 2019. 25 years of DECOVALEX - scientific advances and lessons learned from an international research collaboration in coupled subsurface processes. Int. J. Rock Mech. Min. Sci. 122, 103995.

Briggs, S., Krol, M., 2018. Diffusive transport modelling of corrosion agents through the engineered barrier system in a deep geological repository for used nuclear fuel. NWMO-TR-2018-06. Nuclear Waste Mangement Organization, Toronto, Canada, p. 33.

Briggs, S., McKelvie, J., Keech, P., Sleep, B., Krol, M., 2017a. Transient modelling of sulphide diffusion under conditions typical of a deep geological repository. Corros. Eng. Sci. Technol. 52, 200–203.

Briggs, S., McKelvie, J., Sleep, B., Krol, M., 2017b. Multi-dimensional transport modelling of corrosive agents through a bentonite buffer in a Canadian deep geological repository. Sci. Total Environ. 599–600, 348–354.

Chowdhury, F., Rashwan, T., Papry, S.A., Behazin, M., Keech, P., Mondal, P., Sharma, J., Krol, M., in press-b, Measuring key parameters governing anion transport through MX-80 bentonite. CSCE 2021 Annual Conference. Springer Nature. GEN-308-1-10.

Chowdhury, F., Rashwan, T., Mondal, P., Sharma, J., Krol, M., Behazin, M., Keech P., in press-a. Challenges and lesson learned from experimentally investigating bisulfide diffusion through MX-80 bentonite. GeoNiagara 2021: 74th Canadian Geotechnical Conference and 14th Joint CGS/IAH-CNC Groundwater Conference, Niagara Falls, Canada. 207-1-7.

Cleall, P.J., Melhuish, T.A., Thomas, H.R., 2006. Modelling the three-dimensional behaviour of a prototype nuclear waste repository. Eng. Geol. 85, 212–220.

COMSOL, 2021. Multiphysics® v. 5.6. COMSOL AB, Stockholm, Sweden. www.comsol.com.

Dixon, D.A., 2019. Review of the T-H-M-C Properties of MX-80 Bentonite. NWMO-TR-2019-07. Nuclear Waste Management Organization, Toronto, Canada, p. 197.

Dixon, D.A., Man, A., Rimal, S., Stone, J., Siemens, G., 2018. Bentonite Seal Properties in Saline Water. NWMO TR-2018-20. Nuclear Waste Management Organization, Toronto, Canada, p. 206.

Duro, L., Montoya, V., Colàs, E., García, D., 2010. Groundwater equilibration and radionuclide solubility calculations. NWMO TR-2010-02. Nuclear Waste Management Organization, Toronto, Canada, p. 91.

Einstein, A., 1905. Über die von der molekularkinetischen theorie der Wärme geforderte bewegung von in ruhenden Flüssigkeiten suspendierten teilchen. Ann. Phys. 322, 549–560.

Eriksen, T.E., Jacobsson, A., 1982. Diffusion of hydrogen, hydrogen sulfide and large molecular weight anions in bentonite. TR 17–82. Svensk Kaernbraenslefoersoerjning AB.

Ewing, R.C., 2015. Long-term storage of spent nuclear fuel. Nat. Mater. 14, 252–257.

Gobien, M., Garisto, F., Kremer, E., Medri, C., 2018. Seventh Case Study: Reference Data and Codes. NWMO-TR-2018-10. Nuclear Waste Management Organization, Toronto, Canada, p. 184.

Guo, G., Fall, M., 2021. Advances in modelling of hydro-mechanical processes in gas migration within saturated bentonite: a state-of-art review. Eng. Geol. 287, 106123.

Guo, R., 2016. Thermal response of a Mark II conceptual geological repository in crystalline rock. NWMO-TR-2016-03. Nuclear Waste Management Organization, Toronto, Canada, p. 39.

Guo, R., 2017. Thermal response of a Canadian conceptual deep geological repository in crystalline rock and a method to correct the influence of the near-field adiabatic boundary condition. Eng. Geol. 218, 50–62.

Guo, R., 2018. Thermal response of a conceptual deep geological repository in sedimentary rock. NWMO-TR-2018-09. Nuclear Waste Mangement Organization, Toronto, Canada, p. 47.

Hall, D.S., Behazin, M., Jeffrey Binns, W., Keech, P.G., 2021. An evaluation of corrosion processes affecting copper-coated nuclear waste containers in a deep geological repository. Prog. Mater. Sci. 118, 100766.

Hall, D.S., Keech, P.G., 2017. An overview of the Canadian corrosion program for the long-term management of nuclear waste. Corros. Eng. Sci. Technol. 52, 2–5.

Hall, D.S., Standish, T.E., Behazin, M., Keech, P.G., 2018. Corrosion of copper-coated used nuclear fuel containers due to oxygen trapped in a Canadian deep geological repository. Corros. Eng. Sci. Technol. 53, 309–315.

Huang, Y., Shao, H., Wieland, E., Kolditz, O., Kosakowski, G., 2021. Two-phase transport in a cemented waste package considering spatio-temporal evolution of chemical conditions. npj Mater. Degrad. 5, 4.

Jing, L., Nguyen, T.S., 2005. DECOVALEX III/BENCHPAR PROJECTS. Implications of Thermal-Hydro-Mechanical Coupling on the Near-Field Safety of a Nuclear Waste Repository in a Homogeneous Rock Mass. Report of BMT1B/WP2. Swedish Nuclear Power Inspectorate, Stockholm, Sweden, p. 180.

Kaviany, M., 1995. Principles of Heat Transfer in Porous Media. Springer-Verlag New York, New York.

Keech, P.G., Behazin, M., Binns, W.J., Briggs, S., 2021. An update on the copper corrosion program for the long-term management of used nuclear fuel in Canada. Mater. Corros. 72, 25–31.

Kiczka, M., Pekala, M., Maanoja, S., Muuri, E., Wersin, P., 2021. Modelling of solute transport and microbial activity in diffusion cells simulating a bentonite barrier of a spent nuclear fuel repository. Appl. Clay Sci. 211, 106193.

Kim, C.S., 2017. Evaluation of Coupled Hydro-mechanical (hm) Behaviour of in Situ Shaft Sealing Components for Used Nuclear Fuel. University of Manitoba, Winnipeg, Canada, p. 254 PhD.

King, F., Chen, J., Qin, Z., Shoesmith, D., Lilja, C., 2017a. Sulphide-transport control of the corrosion of copper canisters. Corros. Eng. Sci. Technol. 52, 210–216.

King, F., Hall, D.S., Keech, P.G., 2017b. Nature of the near-field environment in a deep geological repository and the implications for the corrosion behaviour of the container. Corros. Eng. Sci. Technol. 52, 25–30.

King, F., Kolar, M., Maak, P., 2008. Reactive-transport model for the prediction of the uniform corrosion behaviour of copper used fuel containers. J. Nucl. Mater. 379, 133–141.

Martino, T., Partovi-Nia, R., Chen, J., Qin, Z., Shoesmith, D.W., 2014. Mechanisms of film growth on copper in aqueous solutions containing sulphide and chloride under voltammetric conditions. Electrochim. Acta 127, 439–447.

Millard, A., Rejeb, A., Chijimatsu, M., Jing, L., De Jonge, J., Kohlmeier, M., Nguyen, T.S., Rutqvist, J., Souley, M., Sugita, Y., 2004. Evaluation of thm coupling on the safety assessment of a nuclear fuel waste repository in a homogeneous hard rock. In: Stephanson, O. (Ed.), Elsevier Geo-Engineering Book Series. 2. Elsevier, pp. 211–216.

Nasir, O., Fall, M., Nguyen, T.S., Evgin, E., 2015. Modeling of the thermohydromechanical–chemical response of Ontario sedimentary rocks to future glaciations. Can. Geotech. J. 52, 836–850.

Nield, D.A., Bejan, A., 2013. Convection in Porous Media. Springer-Verlag, New York, New York, NY.

NWMO, 2011. OPG's deep geological repository for low and intermediate level wastes: geosynthesis. NWMO DGR-TR-2011-11. Nuclear Waste Management Organization, Toronto, Canada, p. 418.

Pedersen, K., Bengtsson, A., Blom, A., Johansson, L., Taborowski, T., 2017. Mobility and reactivity of sulphide in bentonite clays – implications for engineered bentonite barriers in geological repositories for radioactive wastes. Appl. Clay Sci. 146, 495–502.

Perras, M.A., Diederichs, M.S., 2016. Predicting excavation damage zone depths in brittle rocks. J. Rock Mech. Geotech. Eng. 8, 60–74.

Rutqvist, J., Wu, Y.S., Tsang, C.F., Bodvarsson, G., 2002. A modeling approach for analysis of coupled multiphase fluid flow, heat transfer, and deformation in fractured porous rock. Int. J. Rock Mech. Min. Sci. 39, 429–442.

Shackelford, C.D., Moore, S.M., 2013. Fickian diffusion of radionuclides for engineered containment barriers: diffusion coefficients, porosities, and complicating issues. Eng. Geol. 152, 133–147.

SKB, 2010. Corrosion calculations report for the safety assessment SR-Site. TR-10-66. Svensk Kärnbränslehantering AB, Stockholm, Sweden, p. 52.

Steefel, C.I., Appelo, C.A.J., Arora, B., Jacques, D., Kalbacher, T., Kolditz, O., Lagneau, V., Lichtner, P.C., Mayer, K.U., Meeussen, J.C.L., Molins, S., Moulton, D., Shao, H., Šimůnek, J., Spycher, N., Yabusaki, S.B., Yeh, G.T., 2015. Reactive transport codes for subsurface environmental simulation. Comput. Geosci. 19, 445–478.

Stroes-Gascoyne, S., 2010. Microbial occurrence in bentonite-based buffer, backfill and sealing materials from large-scale experiments at AECL's underground research laboratory. Appl. Clay Sci. 47, 36–42.

Stroes-Gascoyne, S., Hamon, C.J., Maak, P., 2011. Limits to the use of highly compacted bentonite as a deterrent for microbiologically influenced corrosion in a nuclear fuel waste repository. Phys. Chem. Earth A/B/C 36, 1630–1638.

Tait, J.C., Roman, H., Morrison, C.A., 2000. Characteristic and radionuclide inventories of used fuel from OPG Nuclear Generating Stations. Volume 1-main report; and Volume 2-radionuclide inventory data. Ontario Power Generation, Nuclear Waste Management Division. 06819-REP-01200-10029-R00, Toronto, Canada.

van Genuchten, M.T., 1980. A closed-form equation for predicting the hydraulic conductivity of unsaturated soils. Soil Sci. Soc. Am. J. 44, 892–898.

Van Loon, L.R., Glaus, M.A., Müller, W., 2007. Anion exclusion effects in compacted bentonites: towards a better understanding of anion diffusion. Appl. Geochem. 22, 2536–2552.

Van Loon, L.R., Soler, J.M., Bradbury, M.H., 2003. Diffusion of HTO, 36Cl− and 125I− in opalinus clay samples from Mont Terri: effect of confining pressure. J. Contam. Hydrol. 61, 73–83.

Zhou, X., Xu, Y., Da, Sun, Tan, Y., Xu, Y., 2021. Three-dimensional thermal–hydraulic coupled analysis in the nuclear waste repository. Ann. Nucl. Energy 151, 107866.